Iranian Journal of Medical Physics
Vol. 12, No. 3, Summer 2015, 145-166
Received: May 30, 2015; Accepted: September 21, 2015

Original Article

Two Dimensional Mathematical Model of Tumor Angiogenesis: Coupling of Avascular Growth and Vascularization

Farideh Hosseini[1], Nadia Naghavi[*1]

Abstract

Introduction
As a tumor grows, the demand for oxygen and nutrients increases and it grows further if acquires the ability to induce angiogenesis. In this study, we aimed to present a two-dimensional continuous mathematical model for avascular tumor growth, coupled with a discrete model of angiogenesis.
Materials and Methods
In the avascular growth model, tumor is considered as a single mass, which uptakes oxygen through diffusion and invades the extracellular matrix (ECM). After the tumor reaches its maximum size in the avascular growth phase, tumor cells may be in three different states (proliferative, quiescent and apoptotic), depending on oxygen availability. Quiescent cells are assumed to secrete tumor angiogenic factors, which diffuse into the surrounding tissue until reaching endothelial cells. The mathematical model for tumor angiogenesis is consisted of a five-point finite difference scheme to simulate the progression of endothelial cells in ECM and their penetration into the tumor.
Results
The morphology of produced networks was investigated, based on various ECM degradation patterns. The generated capillary networks involved the rules of microvascular branching and anastomosis. Model predictions were in qualitative agreement with experimental observations and might have implications as a supplementary model to facilitate mathematical analyses for anti-cancer therapies.
Conclusion
Our numerical simulations could facilitate the qualitative comparison between three layers of tumor cells, their TAF-producing abilities and subsequent penetration of micro-vessels in order to determine the dynamics of microvascular branching and anastomosis in ECM and three different parts of the tumor.

Keywords: Angiogenesis Factor; Endothelial Cells; Extracellular Matrix; Mathematical Model

1-Department of Electrical Engineering, Faculty of Engineering, Ferdowsi University of Mashhad, Mashhad, Iran
* Corresponding author: Tel: +98 51-38805080; E-mail: n.naghavi@um.ac.ir

1. Introduction

Cancer constitutes a collection of disorders, which share the common feature of uncontrolled cellular growth [1]. Most tissues in the body can give rise to cancer; some can even yield several types of cancer, each with its unique features. The salient feature of cancer cells is that the mechanisms which control growth, proliferation and death of cells are disrupted often due to mutations [1].

Certain types of cancer form solid tumors of aberrant and mutated cells [2]. Development of a primary solid tumor begins with the transformation of a single normal cell as a result of mutation in a certain key gene [3]. Further growth leads to the development of an avascular tumor consisting of approximately 10^6 cells [3]. Initially, a solid tumor relies on diffusion in the adjacent vessels to supply oxygen and nutrients and remove waste products [1]. As the tumor grows, the demand for oxygen and nutrients increases until the flux of oxygen through the tumor surface is too small to supply the entire mass of cells [1]. A necrotic core of dead cells is developed at the center of the tumor, and eventually, the tumor stops growing and remains dormant (diameter of 1-3 mm).

In the tumor, the number of dying cells counterbalances the number of proliferating cells [1]. Tumors only grow further if the cancerous cells acquire one of the so-called hallmarks of cancer, i.e., the ability to induce angiogenesis through mutation [2, 4, 5]. Angiogenesis or neovascularization, which is the formation of blood vessels from a pre-existing vasculature, is a crucial component of many mammalian growth processes [6].

Unlike vasculogenesis, which depends on precursor cells [7], or intussusceptive angiogenesis, which splits the blood vessels [8], angiogenesis is the process through which new blood vessels are formed from pre-existing ones via migration and proliferation mechanisms [2, 9]. Cancer, vascular diseases, stroke, neurodegenerative disorders, diabetes, inflammation, asthma, obesity and arthritis are a group of conditions involving angiogenesis. Angiogenesis also occurs in normal physiology in response to exercise or in the process of wound healing [10].

The first stage of tumor-induced angiogenesis involves the secretion of a number of chemicals into the surrounding tissue through the cells of a solid tumor, collectively known as tumor angiogenesis factors (TAFs) [11]. TAFs diffuse through the tissue space and form a chemical gradient between the tumor and the existing vasculature [6]. Upon reaching any adjacent blood vessels, endothelial cells, lining these vessels, are induced to degrade the basement membranes of the parent vessel and then migrate through the disrupted membranes towards the tumor [6].

The initial response of endothelial cells to TAFs is a chemotactic one, initiating the migration of cells towards the tumor [12]. The cells continue to make their way through the extracellular matrix (ECM), which consists of the interstitial tissue, collagen fiber, fibronectin (FN) and other components.

Among these components, FN is of grave significance in the process of angiogenesis. In fact, FN, as a major component of ECM in both soluble and insoluble forms, is involved in a number of important functions such as wound healing, cell adhesion, blood coagulation, cell differentiation and cell migration [13]. FN in its soluble form (pFN) can be abundantly found in the plasma and other body fluids, while insoluble or cellular FN (cFN) is a major component of ECM [14].

It has been revealed that endothelial cells synthesize and secrete cellular FN, which remains bound to the matrix and does not diffuse [14-18]. The main function of secreted FN is the adhesion of cells to the matrix and directional movements of a number of cell types [19-21]. Therefore, in addition to the chemotactic response of endothelial cells to TAF concentration, there is a complementary haptotactic response to the gradient of adhesiveness in bound FN, termed as haptotaxis [6].

As endothelial cells migrate towards the tumor, they can form loops and branches and

eventually connect with the tumor, penetrate into it, complete the angiogenesis process and supply the tumor with its required nutrients to grow further. Consequently, angiogenesis may provide the possibility for tumor cells to find their way into the circulation and reach secondary sites in the body, resulting in metastasis [3].

A crucial part of the invasive/metastatic process is the ability of cancer cells to degrade the surrounding tissue or ECM [22-24]. The degradation process is a complex mixture of macromolecules, some of which such as collagens are believed to play a structural role and others such as laminin, FN and vitronectin are important for cell adhesion, spreading and motility [3]. A number of matrix degradative enzymes (MDEs) such as the plasminogen activation system (P.4) and the large family of matrix metalloproteinase have been described [25-27].

In recent years, considerable progress has been made in the development of mathematical models, both temporal and spatiotemporal, for tumor growth and angiogenesis, using continuous and discrete approaches. Some of these models have described the avascular tumor growth and its invasion to the surrounding tissue [3, 28-30]. Others have described the most important features of tumor-induced angiogenesis with different approaches ranging from continuous, deterministic frameworks in one-space dimension to discrete, stochastic two-dimensional models [2, 6, 31-39]. Also, in some models, the process of avascular/vascular tumor growth has been coupled with the angiogenesis process [39-41].

In this study, we aimed to couple the tumor angiogenesis process with avascular tumor growth, particularly ECM invasion by tumor cells in the avascular growth stage. The coupling of these two important phases of tumor growth was accomplished by TAFs, secreted from tumor cells under hypoxic conditions. As the tumor reaches its maximum avascular size, three layers with different physiological properties can be recognized. The capillary structures produced in ECM and different tumor layers were investigated in this model.

According to different physiological characteristics of ECM and heterogeneous tumor environment, we estimated two important features of tumor angiogenesis including microvascular branching (MVB) and microvascular anastomosis (MVA), with respect to time. We also examined the relative importance of ECM degradation as a mechanism of invasion in producing different microvascular structures within the tumor and ECM. The model permitted both qualitative and quantitative comparisons with *in vivo* networks.

2. Materials and Methods

2.1. Avascular Tumor Growth and Invasion Model

In this model, we focused on three key parameters: tumor cells, the host tissue (ECM) and MDE associated with tumor cells. The mathematical model consisted of a system of partial differential equations describing ECM degradation by MDE activation and the migratory response of tumor cells.

Initially, we considered a concentration of tumor cells, which grow through the diffusion of oxygen and nutrients from the surrounding tissue. To invade ECM, tumor cells produce MDE, resulting in the destruction of ECM. The invasion model was based on the mathematical model on generic solid tumor growth, which was assumed at the avascular stage for simplicity.

By definition, haptotaxis is the directed migratory response of cells to gradients of fixed or bound chemicals (i.e., non-diffusible chemicals) [3]. Therefore, the directed movement of tumor cells to FN gradients can be determined as follows:

$$J_{hapto} = X\,T\nabla F \qquad (1)$$

Where, $X > 0$ is the constant haptotactic coefficient. T is tumor cell density and ∇F is FN gradient. Another contribution of the invasion model to tumor cell motility is the assumed random motion, a flux of the form:

$$J_{random} = -D_T \nabla \mathrm{T} \qquad (2)$$

Where, D_T is a constant or a function of either MDE or ECM concentration. The conservation equation for tumor cell density (T) is therefore calculated as follows:

$$\frac{\partial T}{\partial t} + \nabla.\left(J_{rand} + J_{hapto}\right) = 0 \qquad (3)$$

The partial differential equation governing the tumor cell motion in the absence of cell proliferation is:

$$\frac{\partial \mathrm{T}}{\partial \mathrm{t}} = \nabla.(\mathrm{D_T(f,m)}\nabla \mathrm{T}) - \mathrm{x_1}\,\nabla.(\mathrm{T}\,\nabla \mathrm{F}) \qquad (4)$$

Where $D_T(f,m)$ is the random motility coefficient of tumor cells. We selected $D_T(f,m) = D_n$ as a constant for the initial simulations.

As noted earlier, MDEs degrade ECM upon contact and therefore, the degradation process can be modeled by the following simple equation:

$$\frac{\partial \mathrm{F}}{\partial \mathrm{t}} = -\delta\,\mathrm{MF}, \qquad (5)$$

Where δ is the ECM degradation coefficient and a positive constant. M is the MDE concentration.

Active MDEs are produced or activated by tumor cells. They diffuse throughout the tissue and undergo some form of decay, either passive or active [3]. The equation governing the evolution of MDE concentration is therefore as follows:

$$\frac{\partial M}{\partial t} = D_M\nabla^2 M + \mu T - \lambda_1 M \qquad (6)$$

Where D_M is the MDE diffusion coefficient and a positive constant, μT denotes MDE production by tumor cells and $\lambda_1 M$ refers to the natural decay of MDE. Therefore, as described earlier, the complete system of equations describing the interactions between tumor cells, ECM and MDEs is:

$$\begin{aligned}
\frac{\partial \mathrm{T}}{\partial \mathrm{t}} &= \overbrace{\mathrm{D_T}\nabla^2\mathrm{T}}^{\text{random motility}} - \overbrace{\mathrm{x_1}\nabla.(\mathrm{T}\nabla\mathrm{F})}^{\text{haptotaxis}},\\
\frac{\partial \mathrm{F}}{\partial \mathrm{t}} &= -\overbrace{\delta\mathrm{MF}}^{\text{degradation}} \qquad (7)\\
\frac{\partial \mathrm{M}}{\partial \mathrm{t}} &= \overbrace{\mathrm{D_M}\nabla^2\mathrm{M}}^{\text{degradation}} + \overbrace{\mu\mathrm{T}}^{\text{production}} - \overbrace{\lambda_1\mathrm{M}}^{\text{decay}}
\end{aligned}$$

To solve the above set of equations numerically, we used dimensionless parameter values for the simulations. We rescaled distance with an appropriate length scale L, time with $\tau_1 = L^2/D_1$ (where D_1 is a reference chemical diffusion coefficient), tumor cell density with $\mathrm{T_0}$, ECM density with $\mathrm{F_0}$ and MDE concentration with $\mathrm{M_0}$ ($\mathrm{T_0}$, $\mathrm{F_0}$, $\mathrm{M_0}$ are appropriate reference variables). Therefore, by setting

$$\tilde{\mathrm{T}} = \frac{\mathrm{T}}{\mathrm{T_0}}, \qquad \tilde{\mathrm{F}} = \frac{\mathrm{F}}{\mathrm{F_0}}, \qquad \tilde{\mathrm{M}} = \frac{\mathrm{M}}{\mathrm{M_0}}, \qquad \tilde{\mathrm{t}} = \frac{\mathrm{t}}{\tau_1}$$

in equation (7) and dropping the tildes for notational convenience, a scaled set of equations was obtained:

$$\begin{aligned}
\frac{\partial \mathrm{T}}{\partial \mathrm{t}} &= \overbrace{\mathrm{d_T}\nabla^2\mathrm{T}}^{\text{random motility}} - \overbrace{\gamma_1\nabla.(\mathrm{T}\nabla\mathrm{F})}^{\text{haptotaxis}},\\
\frac{\partial \mathrm{F}}{\partial \mathrm{t}} &= -\overbrace{\eta_1\mathrm{MF}}^{\text{degradation}}, \qquad (8)\\
\frac{\partial \mathrm{M}}{\partial \mathrm{t}} &= \overbrace{\mathrm{d_M}\nabla^2\mathrm{M}}^{\text{degradation}} + \overbrace{\alpha_1\mathrm{T}}^{\text{production}} - \overbrace{\beta_1\mathrm{M}}^{\text{decay}}
\end{aligned}$$

Where included parameters were defined as follow:

$\mathrm{d\_T} = \mathrm{D\_T} / \mathrm{D\_1}$, $\gamma\_1 = (\mathrm{x\_1\ F\_0}) / \mathrm{D\_1}$, $\eta\_1 = \tau\_1\ \mathrm{M\_0}\ \delta$, $\mathrm{d\_M} = \mathrm{D\_M} / \mathrm{D\_1}$, $\alpha\_1 = (\tau\_1\ \mu\mathrm{T\_0}) / \mathrm{M\_0}$, and $\beta\_1 = \tau\_1\ \lambda\_1$.

It was assumed that tumor cells, and consequently MDEs, remain within the domain of the evaluated tissue, and therefore, no-flux boundary conditions of form (9) for the cells and form (10) for MDEs were imposed on the boundaries of the domain:

$$\underline{\xi}.(-\mathrm{d_T}\nabla\mathrm{T} + \mathrm{T}\gamma_1\nabla\mathrm{F}) = 0 \qquad (9)$$

$$\underline{\xi}.(-\mathrm{d_M}\nabla\mathrm{M}) = 0 \qquad (10)$$

Where $\underline{\xi}$ is an appropriate outward unit normal vector?

For numerical simulations, we discretized the abovementioned system of partial differential equations, using standard finite difference methods. We applied Euler finite difference approximations to discretize the continuous system (8), resulting in the following system [3, 41]:

$$\begin{aligned}
\mathrm{T}_{\mathrm{l,m}}^{\mathrm{q+1}} &= \mathrm{T}_{\mathrm{l,m}}^{\mathrm{q}}\mathrm{P}_0 + \mathrm{T}_{\mathrm{l+1,m}}^{\mathrm{q}}\mathrm{P}_1 + \mathrm{T}_{\mathrm{l-1,m}}^{\mathrm{q}}\mathrm{P}_2\\
&\quad + \mathrm{T}_{\mathrm{l,m+1}}^{\mathrm{q}}\mathrm{P}_3 + \mathrm{T}_{\mathrm{l,m-1}}^{\mathrm{q}}\mathrm{P}_4\\
\mathrm{F}_{\mathrm{l,m}}^{\mathrm{q+1}} &= \mathrm{F}_{\mathrm{l,m}}^{\mathrm{q}}\left[1 - \mathrm{k_1}\eta_1\mathrm{M}_{\mathrm{l,m}}^{\mathrm{q}}\right] \qquad (11)
\end{aligned}$$

$$M_{l,m}^{q+1} = M_{l,m}^{q}\left[1 - \frac{4k_1 D_M}{h^2} - k_1\alpha_1 T_{l,m}^{q}\left(1 - T_{l,m}^{q}\right)\right] + \frac{k_1 D_M}{h^2}\left[M_{l+1,m}^{q} + M_{l-1,m}^{q} + M_{l,m+1}^{q} + M_{l,m-1}^{q}\right]$$

$$P_0 = 1 - \frac{4k_1 D_T}{h^2} - \frac{k_1\gamma_1}{h^2}\left[F_{l+1,m}^{q} + F_{l-1,m}^{q} - 4F_{l,m}^{q} + F_{l,m+1}^{q} + F_{l,m-1}^{q}\right] \quad (12)$$

Where the subscripts specify the location on the grid and the superscripts determine the time steps. Also, *l* and *m* are positive parameters, which specify the position of variables on the two-dimensional grid, i.e., $x = lh$ and $y = mh$. Time discretization is represented by $t = qk_1$.

The coefficient P_0, which is proportional to the probability of no movement, takes the following form [3]:

Also, coefficients P_1, P_2, P_3 and P_4, which are proportional to the probabilities of moving left, right, up and down, take the following forms, respectively:

$$P_1 = \frac{k_1 D_1}{h^2} - \frac{k_1 k\gamma_1}{4h^2}\left[F_{l+1,m}^{q} - F_{l-1,m}^{q}\right] \quad (13)$$

$$P_2 = \frac{k_1 k D_1}{h^2} + \frac{k_1 k\gamma_1}{4h^2}\left[F_{l+1,m}^{q} - F_{l-1,m}^{q}\right] \quad (14)$$

$$P_3 = \frac{k_1 D_1}{h^2} - \frac{k_1\gamma_1}{4h^2}\left[F_{l,m+1}^{q} - F_{l,m-1}^{q}\right] \quad (15)$$

$$P_4 = \frac{k_1 D_1}{h^2} + \frac{k_1\gamma_1}{4h^2}\left[F_{l,m+1}^{q} - F_{l,m-1}^{q}\right] \quad (16)$$

We proposed an initial ECM concentration, which was suitable for the angiogenesis model. We also assumed that the concentration of cellular FN, as a major component of ECM within the tumor, would degrade due to tumor invasion. Based on these assumptions, we considered the following initial conditions for tumor cell, ECM and MDE concentrations, respectively:

$$T(x,y,0)\begin{cases}\exp\left(-\frac{r^2}{\varepsilon_1}\right) & 0 \le r \le 0.1\\ 0 & 0.1 \le r \le 1\end{cases} \quad (17)$$

$$F(x,y,0) = 0.4 - 0.2\,T(x,y,0) \quad (18)$$

$$M(x,y,0) = 0.5\,T(x,y,0) \quad (19)$$

Where r is the radius of the tumor and ε_1 is a positive constant, taken as 0.005 [3, 6].

$$r=\sqrt{(x-1)^2 + (y-0.5)^2} \quad (20)$$

We solved the set of partial differential equations (11) with boundary conditions (9) and (10) and initial conditions (17)-(19), simultaneously.

Experimental studies have indicated that tumors with up to 1-2 mm diameters are usually avascular, while they become vascularized beyond this range [42, 43]. Therefore, we assumed that the angiogenesis process initiates as the tumor reaches its maximum avascular size (~2 mm in diameter). Throughout the process of avascular tumor growth, each tumor cell may be in a different state. By the end of avascular tumor growth, we can distinguish three regions in the tumor. For the simulation of tumor-induced angiogenesis in the computational domain, we assumed that different concentrations of TAF would be secreted by the cells, depending on the region of tumor cells.

2.2. Tumor-Induced Angiogenesis Process

In the angiogenesis model, we focused on three key variables including TAF, FN and endothelial cells. Angiogenesis process consists of a system of partial differential equations, describing FN production and uptake, TAF uptake by endothelial cells and the chemotactic and hepatotoxic effects of endothelial cells in response to TAF and FN gradients, respectively.

We denoted the endothelial cell density per unit area by *n*, TAF concentration by *c* and FN concentration by *f*. The movement of endothelial cells was assumed to be influenced by three factors: random motility, chemotaxis in response to TAF gradient and haptotaxis in response to FN gradient. Therefore, the equation describing the changes in endothelial cell density is as follows [6]:

$$J_{EC} = J_{random} + J_{chemotaxic} + J_{haptotaxic}$$

$$\frac{\partial n}{\partial t} = \nabla . \left[D_n \nabla n - n\,(x(c)\nabla c + \rho_0 \nabla f)\right] \quad (21)$$

Where, D_n, $x(c)$ and ρ_0 denote random migration, chemotaxis and haptotaxis coefficients, respectively. Also, $x(c)$ is a function of form:

$$x(c) = \frac{x_0 k_1}{(k_1 + c)} \quad (22)$$

As mentioned earlier, as soon as TAF is secreted, it diffuses into the surrounding tissue and ECM and sets up a concentration gradient between the tumor and any pre-existing vasculature. We assumed that the steady state of TAF gradient between the tumor and

adjacent vessels could provide the initial conditions for TAF concentration profile. As endothelial cells migrate through ECM in response to this gradient, some TAF uptake and binding occur by the cells. This process can be easily demonstrated by the following consumption function [6]:

$$\frac{\partial c}{\partial t} = -\lambda_2 nc \quad (23)$$

Where λ_2 is a positive constant, representing TAF consumption rate.

Endothelial cells themselves secrete FN, which binds to ECM and does not diffuse. Therefore, an equation, which describes the influence of endothelial cell density on FN concentration, does not contain any diffusion terms. Moreover, there are some connections between FN and endothelial cells as they migrate towards the tumor [14]. FN production and degradation processes can be modeled by the following equation [6]:

$$\frac{\partial f}{\partial t} = wn - \mu_2 nf \quad (24)$$

Where w and μ_2 are positive constants, characterizing the production rate of FN by an individual endothelial cell and degradation of FN, depending on the density of endothelial cells, respectively. Therefore, as partially described in the previous sections, a complete system of equations, describing the response of endothelial cells, TAFs and FN, is as follows:

$$\frac{\partial n}{\partial t} = \overbrace{D_n \nabla^2 n}^{\text{random motility}} - \overbrace{\nabla.\left(\frac{x_0 k_1}{k_1 + c} n \nabla c\right)}^{\text{chemotaxis}} - \overbrace{\nabla.(\rho_0 n \nabla f)}^{\text{haptotaxis}}$$

$$\frac{\partial f}{\partial t} = \overbrace{wn}^{\text{production}} - \overbrace{\mu_2 nf}^{\text{uptake}} \quad (25)$$

$$\frac{\partial c}{\partial t} = -\overbrace{\lambda_2 nc}^{\text{uptake}}$$

In order to solve the above system of equations numerically, dimensionless parameter values were used for the simulations. We rescaled distance with L (the distance between the parent vessel and tumor), time with $\tau_2 = L^2/D_C$ (where D_c is the TAF diffusion coefficient), endothelial cell density with n_0 and TAF and FN concentrations with c_0 and f_0, respectively (where n_0, c_0 and f_0 are appropriate reference variables). Therefore, a non-dimensional system was obtained as follows [6]:

$$\frac{\partial n}{\partial t} = \nabla.[D_2 \nabla n - n\left(\frac{x_2}{1+\alpha_2 c}\nabla c + \rho \nabla f\right)]$$

$$\frac{\partial c}{\partial t} = -\eta_2 nc \quad (26)$$

$$\frac{\partial f}{\partial t} = \beta_2 n - \gamma_2 nf$$

And parameters were defined as follows:

$$D=\frac{D_n}{D_c}, \quad x = \frac{x_0 c_0}{D_c}, \alpha_2 = \frac{c_0}{k_1}, \quad \rho = \frac{\rho_0 f_0}{D_c}, \quad \beta = \frac{wL^2 n_0}{f_0 D_c}, \quad \gamma = \frac{\mu_2 L^2 n_0}{D_c}, \quad \eta = \frac{\lambda_2 L^2 n_0}{D_c} \quad (27)$$

No-flux conditions were imposed on the boundaries of the unit square for endothelial cells:

$$\underline{\xi}.(-D_2 \nabla n + n\,(x(c)\nabla c + \rho \nabla f)) = 0 \quad (28)$$

It should be noted that no boundary conditions can be imposed on c and *f*.

As mentioned earlier, for the most internal cells of tumor, oxygen concentration is below the critical threshold and hypoxia leads to cell apoptosis; therefore, these cells secrete TAF at a lower level. The next layer of the tumor includes quiescent (hypoxic) cells, which do not proliferate and die in case oxygen concentration is insufficient for the cells. In this state, the cells produce the highest level of TAF, which diffuses into the surrounding tissue until it reaches the endothelial cells [44]. TAF secretion is due to the fact that in the steady state, the number of living cells, which compete for oxygen, increases, resulting in the increased demand for oxygen.

The outer layer of the tumor consists of proliferative cells. Oxygen concentration is sufficient for these cells to proliferate and they can progress through the cell cycle and duplicate [44]; therefore, cells in this layer do not secrete any TAFs. We estimated the initial TAF concentration in the steady state in different tumor regions to model this condition.

We considered three different profiles for the initial TAF concentration in the angiogenesis model. These profiles included a relatively constant low level of TAF with a radius of 0.1 (showing necrotic cells), a continuous ascending profile indicating TAF production

by quiescent (hypoxic) cells and a continuous descending TAF profile showing the diffusion of TAF, secreted by hypoxic cells into the surrounding tissue.

In this study, we considered two different steady state profiles for the initial FN concentration in order to determine the inner and outer regions of the tumor, respectively. We also assumed that FN concentration (as a major macromolecule of ECM) inside the tumor region is equivalent to ECM, destroyed as a result of avascular tumor growth. Therefore, we used the ECM concentration from the tumor invasion model (described in section 2.1) for determining FN concentration in the tumor region. A descending exponential function was also used to model both cellular and plasma FN concentrations in the steady state in ECM. Therefore, the initial condition for TAF concentration was as follows:

$$c(x,y,0)=\begin{cases}0.7071 & 0\le r\le 0.1\\ \frac{v-0.5884}{v-r} & 0.1\le r\le 0.3\\ \left(\frac{v-r}{v-0.1294}\right)^2 & 0.3\le r\le 1\end{cases} \quad (29)$$

Where r is defined as equation (20) and v is defined as follows:

$$v=\frac{\sqrt{5}-0.1}{\sqrt{5}-1} \quad (30)$$

The initial condition for FN was also described:

$$f(x,y,0)=\begin{cases}\text{concentration of ECM from the avascular growth model} & 0\le r\le 0.5\\ Ke^{-\frac{(x)^2}{\varepsilon_2}} & 0.5\le r\le 1\end{cases} \quad (31)$$

Where K and ε_2 are positive constants, calculated to be 0.75 and 0.45, respectively [6].

The discrete model of angiogenesis incorporated rules for sprout branching and anastomosis and contained an element of stochasticity for the movement of cells. This discrete model was derived from a discretized form of partial differential equations of the system (25). By using the Euler finite difference methods [41], the resulting coefficients of the five-point finite difference stencil were used to determine the probability of the movement of an individual cell in response to its local milieu. The full discretized model is described as follows [6]:

$$\begin{aligned} n_{l,m}^{q+1} &= n_{l,m}^{q}P_0 + n_{l+1,m}^{q}P_1 + n_{l-1,m}^{q}P_2 + n_{l,m+1}^{q}P_3 + n_{l,m-1}^{q}P_4\\ f_{l,m}^{q+1} &= f_{l,m}^{q}\left[1-k_2\gamma_2 n_{l,m}^{q}\right] + k\beta_2 n_{l,m}^{q} \quad (32)\\ c_{l,m}^{q+1} &= c_{l,m}^{q}\left[1-k_2\eta_2 n_{l,m}^{q}\right] \end{aligned}$$

Where the subscripts specify the location on the grid and the superscripts specify the time steps. Also, l and m are positive parameters, which specify the position of variables on the two-dimensional grid, i.e., $x=lh$ and $y=mh$. Time discretization was represented by $t=qk_2$. The exact forms of P_0–P_4 involve functions of FN and TAF concentrations in the vicinity of an individual endothelial cell [6]. These coefficients can be thought to be proportional to the probability of endothelial cell being stationary (P_0) or moving left (P_1), right (P_2), upward (P_3) or downward (P_4). The coefficient P_0, which is proportional to the probability of no movement, takes the following form:

$$\begin{aligned} P_0 = 1 &- \frac{4k_2D_2}{h^2} + \frac{k_2\alpha_2 x\left(c_{l,m}^{q}\right)}{4h^2\left(1+\alpha_2 c_{l,m}^{q}\right)}\left[(c_{l+1,m}^{q}-c_{l-1,m}^{q})^2 + (c_{l,m+1}^{q}-c_{l,m-1}^{q})^2\right] - \frac{k_2 x\left(c_{l,m}^{q}\right)}{h^2}\left(c_{l+1,m}^{q}+c_{l-1,m}^{q}-4c_{l,m}^{q}+c_{l,m+1}^{q}+c_{l,m-1}^{q}\right) - \frac{k_2\rho}{h^2}\left(f_{l+1,m}^{q}+f_{l-1,m}^{q}-4f_{l,m}^{q}+f_{l,m+1}^{q}+f_{l,m-1}^{q}\right) \quad (33)\\ P_1 &= \frac{k_2 D}{h^2} - \frac{k_2}{4h^2}\left[x\left(c_{l,m}^{q}\right)\left(c_{l+1,m}^{q}-c_{l-1,m}^{q}\right)+\rho\left(f_{l+1,m}^{q}-f_{l-1,m}^{q}\right)\right] \quad (34)\\ P_2 &= \frac{k_2 D}{h^2} + \frac{k_2}{4h^2}\left[x\left(c_{l,m}^{q}\right)\left(c_{l+1,m}^{q}-c_{l-1,m}^{q}\right)+\rho\left(f_{l+1,m}^{q}-f_{l-1,m}^{q}\right)\right] \quad (35)\\ P_3 &= \frac{k_2 D}{h^2} - \frac{k_2}{4h^2}\left[x\left(c_{l,m}^{q}\right)\left(c_{l,m+1}^{q}-c_{l,m+1}^{q}\right)+\rho\left(f_{l,m+1}^{q}-f_{l,m-1}^{q}\right)\right] \quad (36)\\ P_4 &= \frac{k_2 D}{h^2} + \frac{k_2}{4h^2}\left[x\left(c_{l,m}^{q}\right)\left(c_{l,m+1}^{q}-c_{l,m+1}^{q}\right)+\rho\left(f_{l,m+1}^{q}-f_{l,m-1}^{q}\right)\right] \quad (37) \end{aligned}$$

2.2.1. Sprout Branching and Anastomosis

Branching, as a process through which new sprouts are formed from capillary cells, and anastomosis, a process by which tip cells from one sprout merge with capillary cells from

another sprout, were explicitly incorporated to the discrete model. By meeting the following three conditions, a capillary sprout can branch at its tip and generate a new sprout [6]:

1. The age of the current sprout should be greater than the age of threshold branching Ψ (equivalent to a dimensional time of 0.75 days).
2. Sufficient space should locally exist for a new sprout to form (we assumed a forward diagonal branching pattern).
3. The endothelial cell density should be greater than the threshold level n_b ($n_b \propto \frac{1}{c_{l,m}}$).

If all these three conditions were satisfied, each sprout tip was assumed to have a probability P_b, of generating a new sprout (branching); this probability was dependent on the local TAF concentration. The sprout branching probabilities, associated with various TAF concentration ranges, were selected on a qualitative basis, as presented in Table 1 [6].

As the sprouts progress towards the tumor, driven by the movement probabilities presented in (31) at each time step of the simulation, endothelial cells at the sprout tips can move to any four orthogonal neighbors on the discrete grid. If during one of these movements, another sprout is encountered, anastomosis may occur [6]. The schematic diagram for sprout branching and anastomosis is presented in Figure 1.

3. The simulation analysis

The simulations of the model were carried out on a 200× 200 grid, which is a discretization of the unit square [0, 1] × [0, 1], with a space step of h =0.005, representing a tissue with dimensions of [0, 2 mm] × [0, 2 mm]. We assumed that the tumor has reached its maximum pre-vascular growth state, which is equivalent to a tumor with 0.5 radius on the dimensionless unit square (equal to a tumor with a radius of 1 mm), and is centered at *x=1* and *y=0.5*.

Table1. Sprout tip branching probabilities as a function of local TAF concentration [6]

TAF concentration	Sprout tip branching probability
≤0.3	0.0
[0.3-0.5]	0.2
[0.5-0.7]	0.3
[0.7-0.8]	0.4
[0.8-1]	1

[TAF: Tumor angiogenesis factor]

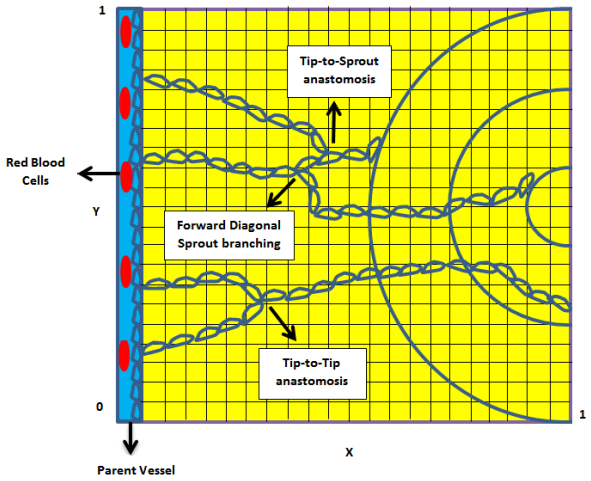

Figure 1.The schematic diagram for sprout branching and anastomosis

Figure 2 presents the schematic diagram of the model domain, including the multi-layered tumor on the right boundary of the domain, endothelial cells lining the parent blood vessel on the left boundary and ECM located in between. According to our unit of 2 mm length, discretization of a unit square with a space step of h =0.005 implied that h is equivalent to a dimensional length of 10 μm, i.e., approximately the length of one or two endothelial cells [6, 45].

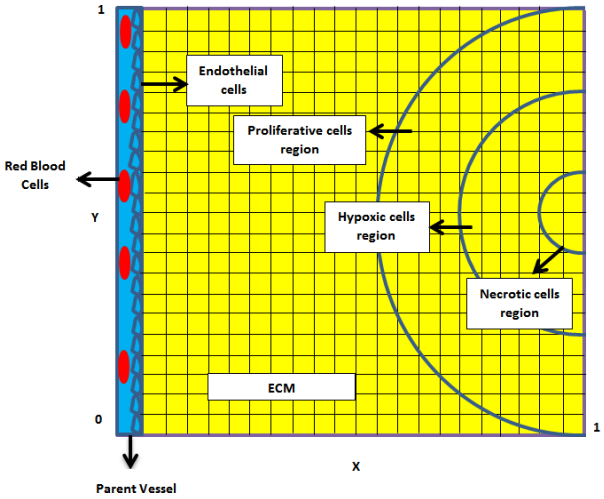

Figure 2. The schematic diagram of the model domain including a parent blood vessel, a multi-layered tumor and endothelial cells lining the blood vessel. The discretization of the simulation domain is also illustrated.

All numerical solutions presented in this section were obtained from finite difference approximations in systems (8) and (25) with boundary and initial conditions (9)-(10) and (17)-(19) for the avascular tumor growth model and conditions (28) and (29)-(31) for the angiogenesis model, respectively. The iterative steps for the numerical simulations were as follows (Figure 3):

Step 1: We set the boundary and initial conditions for the avascular tumor growth model as given in equations (9)-(10) and (17)-(19), respectively.

Step 2: We solved the discrete system (11) numerically for each time step of the simulation process to obtain F and M values and then generated the five coefficients P_0–P_4, according to equations (12)-(16).

Step 3: We updated the value of T from the five generated coefficients (P_0–P_4) for each point of the domain at each time step.

Step 4: The data obtained from this model were applied as some initial conditions for coupling with the angiogenesis model at the time of maximum avascular tumor growth. In this step, we set the degraded ECM concentration as the initial FN concentration inside the tumor and the initial TAF concentration was determined, based on the progression of tumor cells in this situation. Moreover, we set the boundary and initial conditions for the angiogenesis model as given in (28) and (29)-(31), respectively. We also assumed that five sprouts, located randomly along the parent vessel, were initially activated by TAF.

Step 5: We solved the discrete system of (32) numerically for each time step of the angiogenesis simulation process to obtain the values of f and c and then generated the coefficients P_0–P_4, according to equations (33)-(37).

Step 6: We computed the probability ranges by summing the coefficients P_0–P_4 to produce five ranges: $R_0 = [0, P_0]$ and $R_j = [\sum_{i=0}^{j-1} P_i\ ,\ \sum_{i=0}^{j} P_i]$ $(j = 1 - 4)$. Then, we generated a random number between 0 and 1. The individual endothelial cell remained stationary or moved left, right, up or down if the random number fell in R_0, R_1, R_2, R_3 or R_4 ranges, respectively. Therefore, each endothelial cell was restricted to move to one of its four orthogonal neighboring grid points or remain stationary at each time step.

Step 7: We assessed the conditions for sprout branching or anastomosis in each time step.

Step 8: We assessed the stop criteria. In this step, if the vessels reached the end of the network, the process ended; otherwise, the program continued to step 5.

Parameter values used in the simulations were dimensionless, as presented in Table 2. Figure 4 shows the initial conditions for tumor cell, MDE and ECM concentrations, used in the avascular tumor growth model.

Table 2. The summary of model parameters

Parameters	Description	Value*	Equation	Reference
d_T	Tumor cell motility	0.001	(8)	[3]
d_M	MDE diffusion coefficient	0.001	(8)	[3]
γ_1	Tumor haptotactic coefficient	0.005	(8)	[3]
η_1	ECM degradation	10	(8)	[3]
α_1	MDE production	0.1	(8)	[3]
β_1	MDE decay	0	(8)	[3]
D_2	EC random motility coefficient	0.00035	(26)	[6]
x_2	EC chemotactic coefficient	0.38	(26)	[6]
ρ	EC haptotactic coefficient	0.34	(26)	[6]
η_2	TAF uptake	0.1	(26)	[6]
β_2	Fibronectin production	0.05	(26)	[6]
γ_2	Fibronectin uptake	0.1	(26)	[6]
α_2	Chemotactic sensitivity coefficient	0.6	(26)	[6]

*All values are dimensionless. [MDE: matrix degradative enzyme, ECM: extracellular matrix, EC: endothelial cell, TAF: tumor angiogenesis factor]

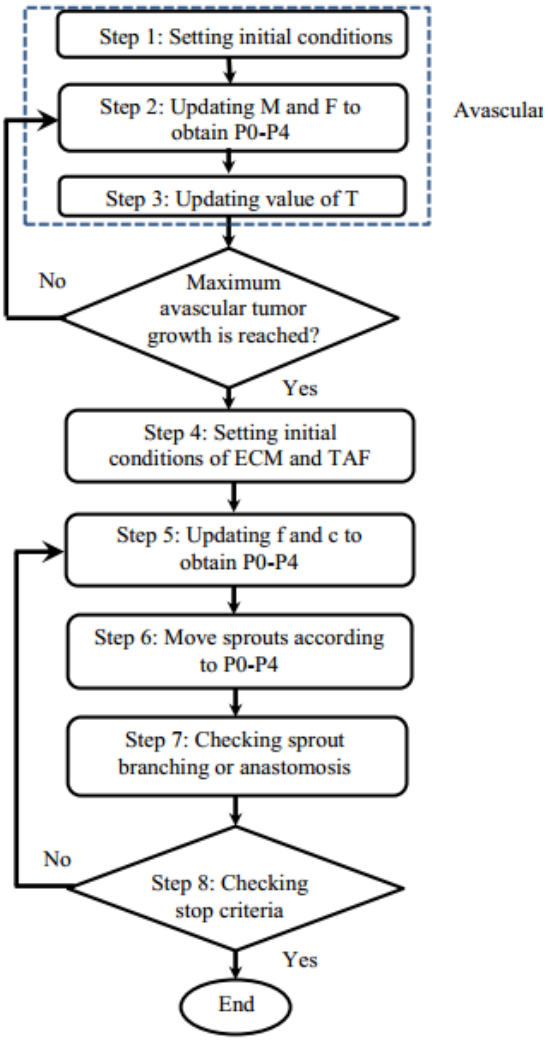

Figure 3. The flow chart of iterative steps for numerical simulations of the model

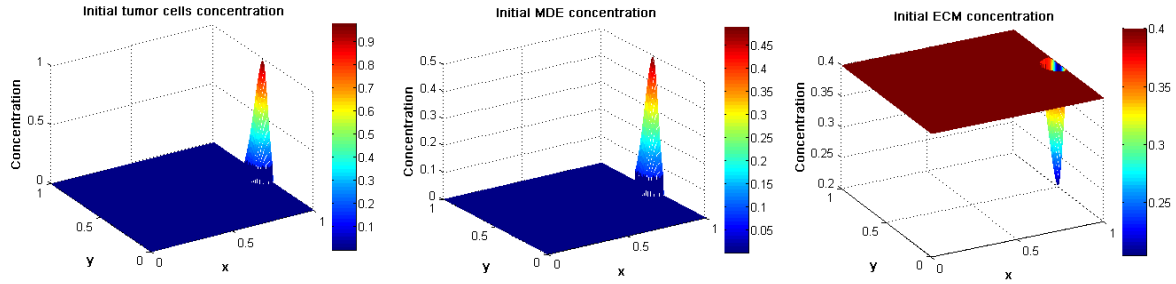

Figure 4. The initial conditions for tumor cell, matrix degradative enzyme (MDE) and extracellular matrix (ECM) concentrations, used in the avascular tumor growth model

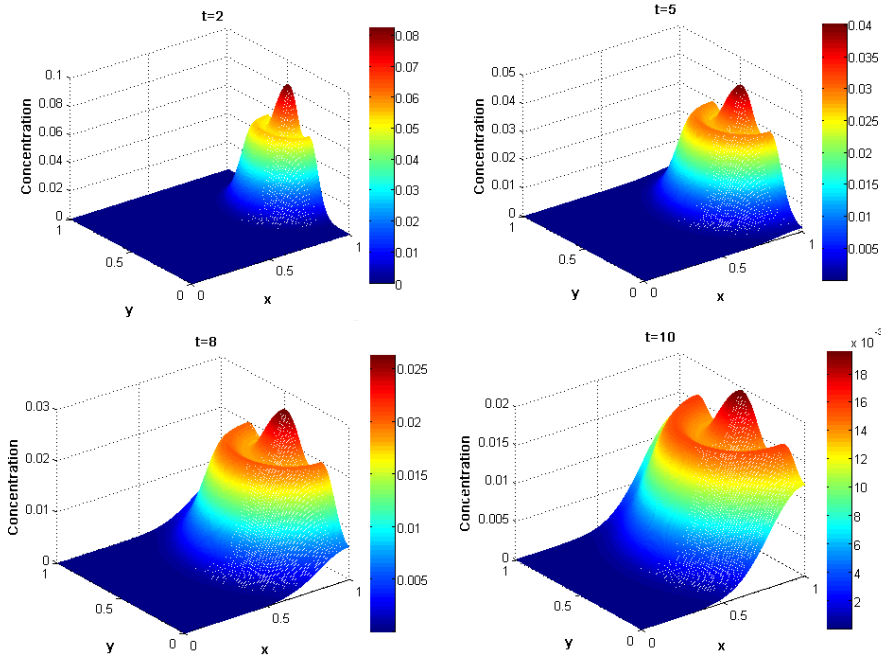

Figure 5. Spatiotemporal evolutions of tumor cell invasion, resulting from the numerical simulation of the system (8)

3. Results

As mentioned earlier, we first ran the avascular tumor growth code to obtain the concentrations of the three set variables at the time of maximum avascular tumor growth. Figure 5 indicates the gradual tumor cell growth and invasion in four snapshots at the time of tumor cell density distribution. As expected, the main body of the tumor slowly invaded due to haptotactic migration. At the leading edge, a region of higher cell density was detected, which could gradually break into two separate clusters. As tumor cells grew, they produced MDE to degrade the surrounding tissue. Figures 6 and 7 represent the gradual changes in the MDE and ECM concentrations for the corresponding time in Figure 5. The ECM profile clearly indicates its degradation by MDEs.

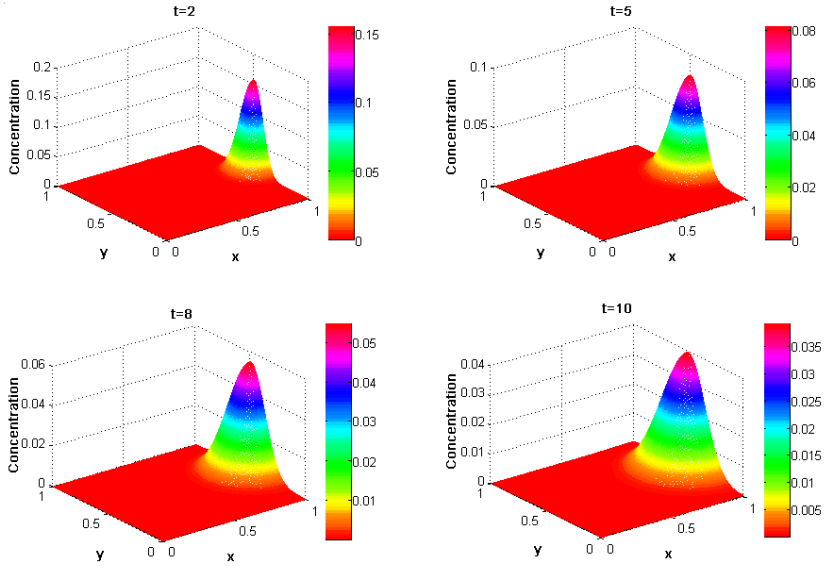

Figure 6. Spatiotemporal evolutions of matrix degradative enzymes (MDEs), resulting from the numerical simulation of the system (8)

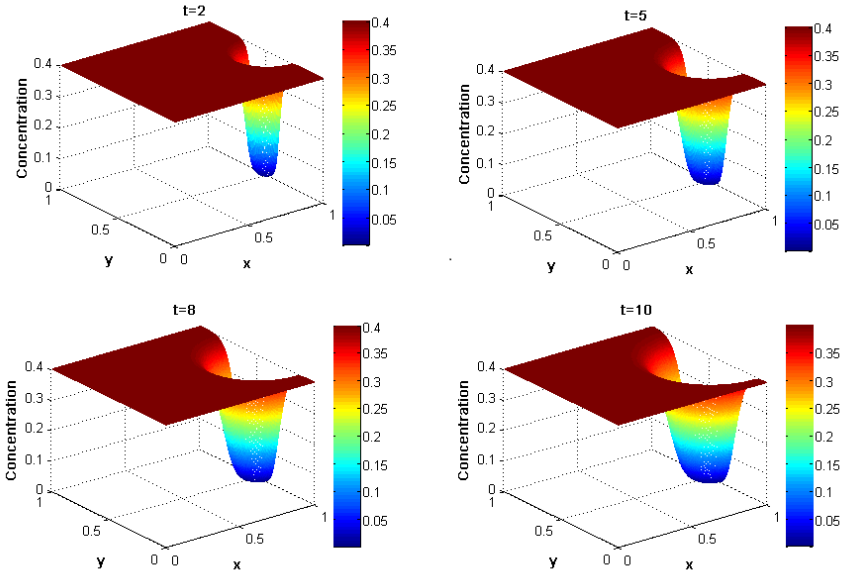

Figure 7. Spatiotemporal evolutions of extracellular matrix (ECM), resulting from the numerical simulation of the system (8)

At time t=10 (46 days), the tumor reached the edge of the domain, which was equal to a tumor with a 2 mm diameter. As mentioned earlier, in this situation, the demand for oxygen and nutrients by tumor cells is beyond diffusion from the surrounding tissue; consequently, tumor cells cease to grow. Hypoxic tumor cells start to secrete TAF for initiating the angiogenesis process. The TAF secreted by hypoxic tumor cells diffuses in the ECM to reach the neighboring blood vessels. Therefore, there is a delay between the time of maximum avascular tumor growth and the initial angiogenesis.

The mentioned time interval is proportional to multiple factors such as TAF diffusion coefficient, TAF degradation rate and the distance between the tumor and blood vessel. After this time interval, sprouts slowly initiate and the process of angiogenesis starts. We

assumed that TAF has reached its steady-state concentration at the start of angiogenesis. Therefore, the concentration of TAF, secreted by hypoxic cells, at the steady state was regarded as the initial TAF concentration for the angiogenesis model.

We also assumed that plasma FN diffuses from the parent vessel in response to the destruction of vascular basement membrane. The initial conditions for TAF and FN are demonstrated in Figure 8. Figure 9 indicates the spatiotemporal evolution of five sprout tips, depicted by the numerical simulation of the coupled model.

At t=1, i.e., 1.5 days after the initiation of angiogenesis and 47.5 days after the initiation of avascular tumor growth (we assumed no delay between the time when the tumor reached its maximum avascular size and the initiation of angiogenesis), the sprouts grew nearly in parallel with each other and formed some orders of branching without any anastomosis. Once the sprouts reached a certain distance from the parent vessel, they tended to incline towards each other and finally formed tip-to-tip and tip-to-sprout fusions at about t=3, i.e., 4.5 days after the initiation of angiogenesis and 50.5 days after the initiation of avascular tumor growth.

Due to the circular geometry of TAF concentration profile and the effect of chemotaxis in the model, the sprouts and their branches converged towards the middle of the domain until t=5 (53.5 days after avascular tumor growth). As expected, the model could follow the "brush-border" effect, due to the increased frequency of branching at the edge of the network as the capillary sprouts approached the tumor. This procedure was reported by Folkman et al. [11, 43] and our results followed their experimental findings.

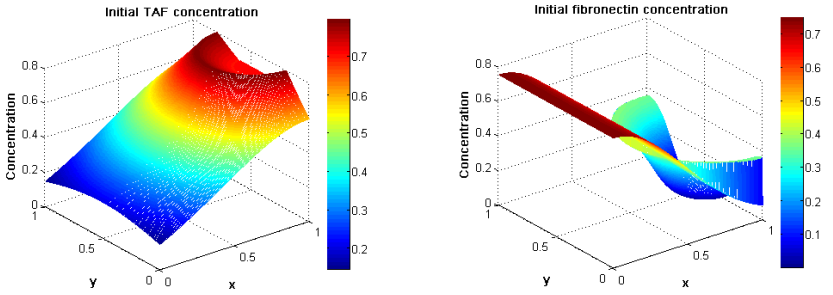

(a) (b)

Figure 8. The initial concentrations of (a) tumor angiogenesis factor (TAF) in the multi-layered tumor and (b) fibronectin (FN) for the initiation of angiogenesis

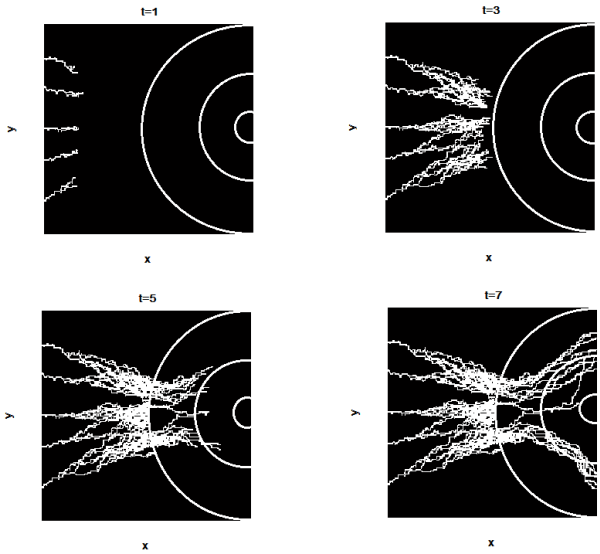

Figure 9. Spatiotemporal evolutions of sprout tips, resulting from the numerical simulation of the coupled model

Some orders of capillary branching and anastomosis were reported by t=3. Expectedly, the brush-border effect on the boundary of the tumor was observed at t=5. Some micro-vessels penetrated into the tumor and converged to the center of the domain. These micro-vessels then distributed around the region of hypoxic tumor cells due to the uniform concentration of TAF in this area and insufficient FN concentration. A few micro-vessels might have also entered the necrotic region.

One of the interesting findings of our simulations was that the number of micro-vessels, penetrating into the tumor, was not in balance with the outer micro-vessels. Therefore, when ECM degradation was significant, the newly formed vessels tended to encapsulate rather than penetrate the tumor; therefore, they were less effective in delivering nutrients [31]. This micro-vessel, settling down on the surface of the tumor, could cause some problems in the treatment process, as well.

The high number of redundant micro-vessels, which do not penetrate into the tumor, can change the dilution of delivered drugs and influence the efficiency of treatment. As depicted in Figure 9, some sprouts settled down on the edge of the tumor at t=5 and did not penetrate into the tumor until the end of simulation. Although the sprouts remained on the tumor boundary, others penetrated into the tumor and produced a high density of capillaries in the region of proliferative cells and converged towards the middle of the domain in response to TAF, secreted by semi-necrotic (hypoxic) cells.

After penetration into the hypoxic cell region, capillary vessels distributed around the hypoxic cells, given the uniform concentration of TAF and insufficient FN concentration. A few micro-vessels might have also entered the necrotic region. The three regions of the tumor changed to well-, semi- and non-vascularized regions after the angiogenesis process.

In order to investigate the effect of ECM degradation coefficient η_1 on microvascular structures within the tumor, the coefficient was increased by a factor of 5, i.e., η_1=50, representing the increased ECM degradation by MDEs, produced throughout tumor cells. By using the same parameters presented in Figure 5, the four snapshots in Figures 10 and 11 were produced.

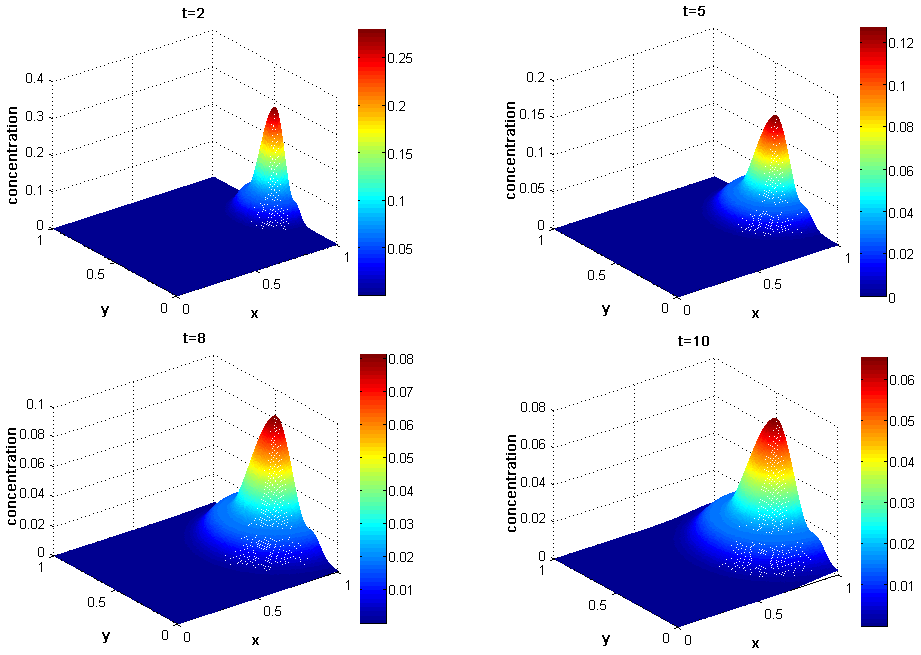

Figure 10. Spatiotemporal evolutions of tumor cell invasion, resulting from the numerical simulation of the system (8) with parameter values mentioned in Figure 5 (exceptfor η_1=50)

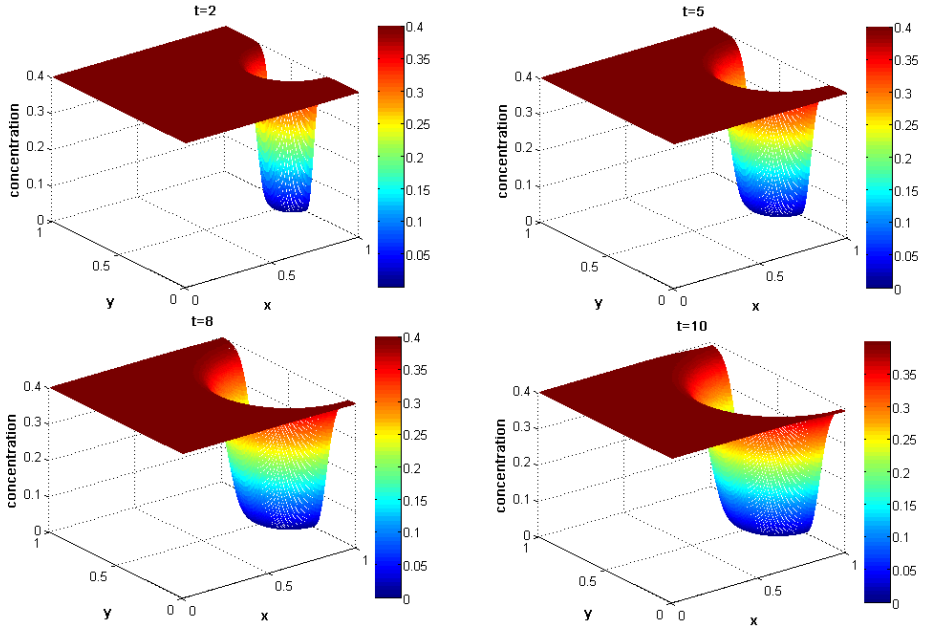

Figure 11. Spatiotemporal evolutions of extracellular matrix (ECM), resulting from the numerical simulation of the system (8) with parameter values, depicted in Figure 5 (except for η_1=50)

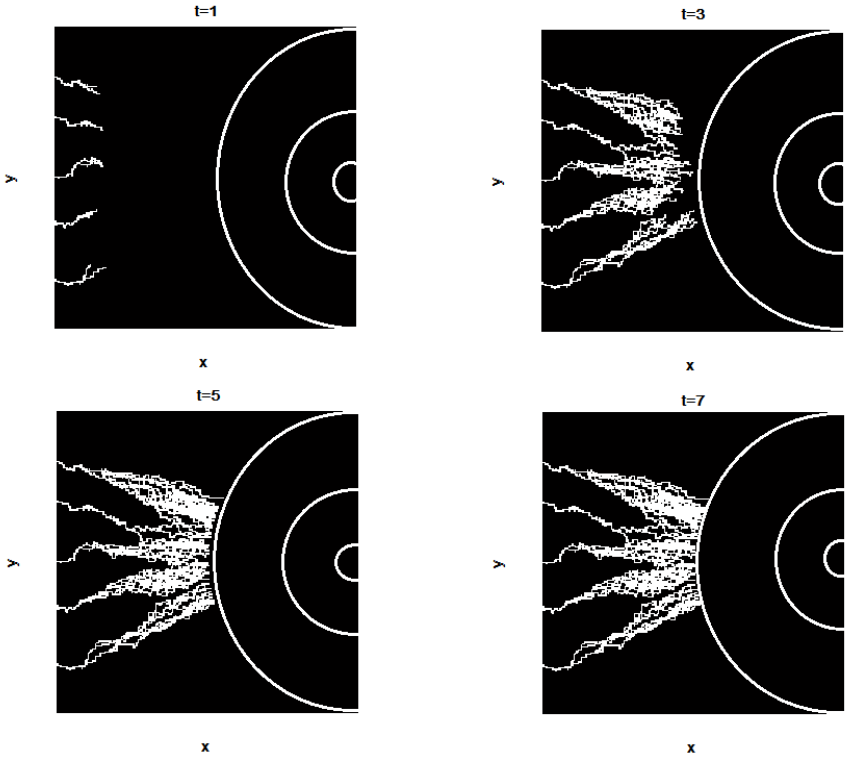

Figure 12. Spatiotemporal evolutions of sprout tips, resulting from the numerical simulation of the coupled model with parameter values, depicted in Figure 9 (except for η_1=50). The brush-border effect was observed on tumor boundary at t=5; however, due to the significant degradation of ECM, micro-vessels did not penetrate into the tumor.

In this case, tumor cells remained more localized and did not invade the tissue as much. The initiation of angiogenesis process with this data resulted in the production of a capillary structure, as depicted in Figure 12. In this situation, ECM degradation by MDEs was significant, and therefore, all newly formed vessels tended to settle down on the tumor boundary and not penetrate into the tumor. This property of microvascular structures not only causes some problems in nutrient

delivery, but also challenges the treatment process.

As shown in Figure 13, we investigated the effect of decreasing ECM degradation coefficient rate η_1 by a factor of 100, i.e., η_1=0.1, on the tumor invasion pattern. The results indicated a considerable change in tumor density distribution. At t=2, a small cluster of cells migrated slowly from the main body of the tumor and continued to invade ECM at the leading edge.

As illustrated in Figure 13, particularly Figure 14, decreased ECM degradation coefficient rate η_1 resulted in a slower invasion of ECM by tumor cells in a way that the tumor did not reach its maximum avascular size at t=10. By increasing the duration of simulation to about t=12, maximum tumor size was reported at the end of the avascular growth phase. Figure 15 represents the produced microvascular structure in this model. In this case, all micro-vessels on the boundary entered the tumor with a high density of branching and anastomosis in the region of proliferative cells. Despite the high concentration of TAF in the hypoxic tumor cells, none of the micro-vessels entered this region due to insufficient FN concentration in ECM. The sharp descending edge of ECM in Figure 14 represents the high level of ECM degradation in this region. MDE concentration profiles in the last two simulations closely resembled those obtained in Figure 6, unless some changes were reported in concentration values.

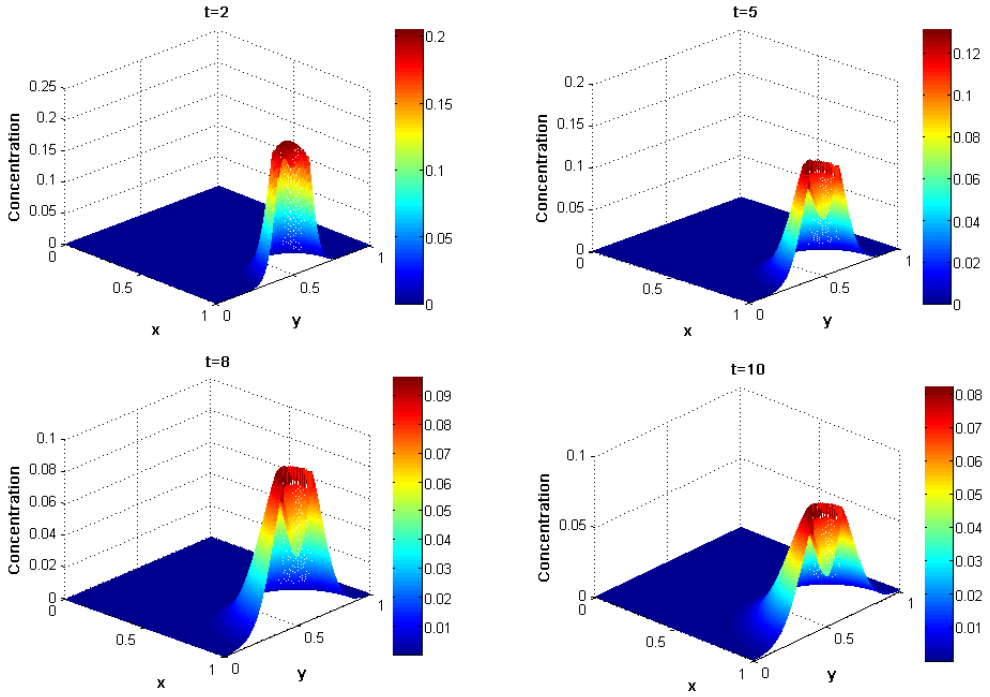

Figure 13. Spatiotemporal evolutions of tumor cell invasion, resulting from the numerical simulation of the system (8) with parameter values, depicted in Figure 5 (except for η_1=0.1)

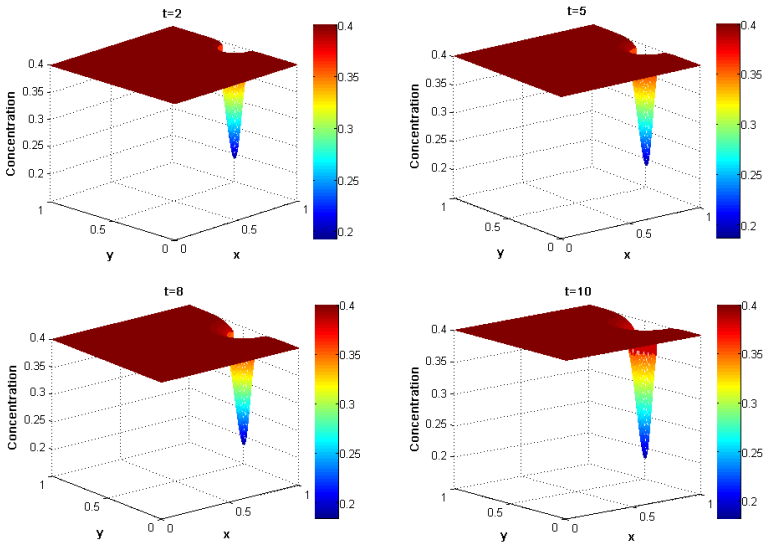

Figure 14. Spatiotemporal evolutions of extracellular matrix (ECM), resulting from the numerical simulation of the system (8) with parameter values, depicted in Figure 5 (except for η_1=0.1)

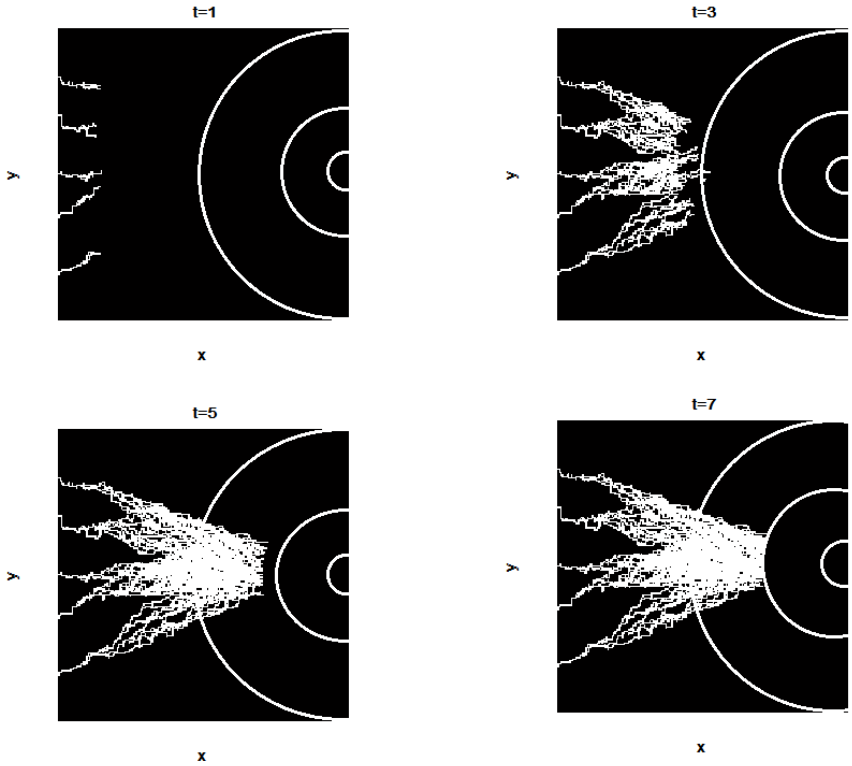

Figure 15: Spatiotemporal evolutions of sprout tips, resulting from the numerical simulation of the coupled model with parameter values as depicted in Figure 9 (except for η_1=0.1)

The brush-border effect on the tumor boundary was observed at t=5. There was a balance between the number of micro-vessels on the tumor boundary and micro-vessels penetrating into the tumor. However, the significant degradation of ECM in the region of hypoxic tumor cells prevented micro-vessels from penetrating the hypoxic cell region.

As mentioned earlier, the produced capillary network was complex with a high density of branching and anastomosis, which are important structural features in the treatment process. The high level of branching leads to the dilution of drug delivered to the tumor and can affect the efficiency of treatment. The number of microvascular loops or anastomosis

inside the tumor can also affect the amount of drug delivered to the tumor.

In Figure 16, we estimated the probability of MVB in ECM and different parts of the tumor, with respect to time $\eta_1 = 10$. As illustrated, at t=5, i.e., 7.5 days after the initiation of angiogenesis and 53.5 days after avascular tumor growth, the highest degree of branching occurred at the outer edge of the tumor, which shows the brush-border effect in proliferative cells. Also, a well-vascularized area was formed at the most outer layer of the tumor.

This extensive new capillary bed can supply not only the nutrients for the rapid growth of tumor tissues, but also the metastatic pathways for tumor cells. Therefore, the high branching rate on the edge of the tumor reduces the efficiency of drugs delivered to the tumor, while the high branching rate within the tumor increases the probability of tumor cell migration.

There was also a lower level of new branching in the hypoxic region, which shows that all the vessels, which entered this region, continued to progress without any new branching patterns. This probability was equal to zero for the necrotic region, which is due to the absence of any micro-vessels in this area.

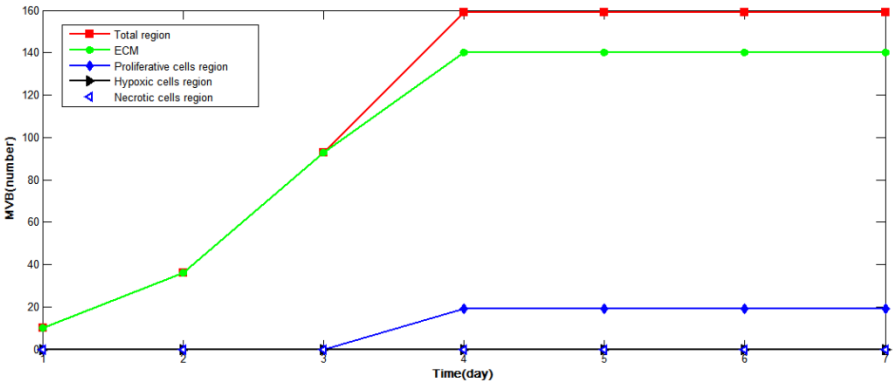

Figure 16: Comparison of microvascular branching in the extracellular matrix (ECM) and different parts of the tumor. It can be observed from the "total region" plot that the maximum branching occurred between t=3 and t=4, indicating the brush-border effect at the outer edge of the tumor.

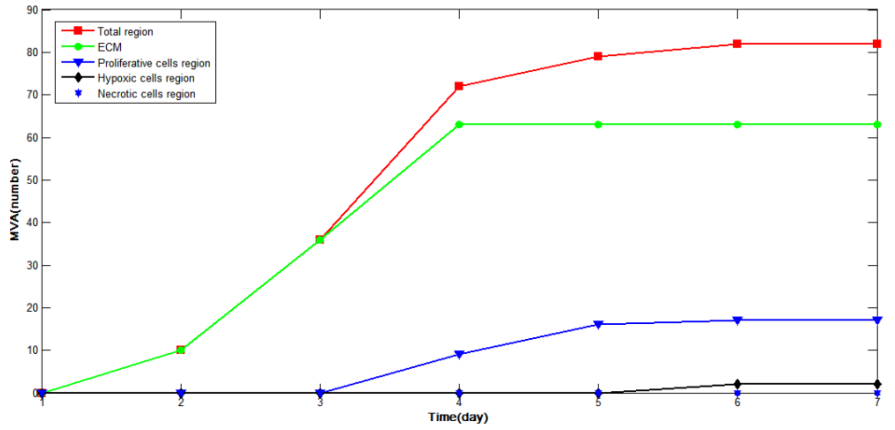

Figure 17. The number of microvascular anastomosis (MVA) in different parts of the simulation area

Figure 17 shows the number of MVA with respect to time in different parts of the simulation area. There were some orders of anastomosis in different regions, except the necrotic cell region. Some of these formed loops within the tumor facilitated blood circulation and exchange of oxygen, nutrients or even drugs. Other loops occurred in ECM

and bypassed the drug, with no significant effects on tumor growth. As depicted in Figure 17, a large number of loops were present in ECM, which is one of the important causes of failure in drug treatment.

4. Discussion

Phenomenological models can provide a framework for understanding physical systems, exploring the effects of different hypotheses and advancing our conceptual understanding and even our predictive abilities. In this study, we investigated the process of tumor growth, using an avascular tumor growth model, coupled with a tumor-induced angiogenesis model. These coupled mathematical models enable us to have a better estimation of tumor invasion state.

We developed the tumor angiogenesis model, based on the model proposed by Anderson and Chaplain [6]. However, we modified the initial conditions for FN and TAF concentrations in order to simulate microvascular structures inside and outside the tumor. For this purpose, we first simulated the avascular tumor growth to obtain the ECM degradation profile within the tumor region and used the data provided by this simulation to initiate the tumor angiogenesis process.

Simulation of avascular tumor growth not only presents some of the initial conditions for the angiogenesis model, but also provides an appropriate estimation of the spatiotemporal progression of solid tumors. We simulated a multi-layered tumor, consisting of three different layers at the steady state during maximum avascular growth, based on TAF concentration released by hypoxic cells in the middle layer. Moreover, the morphology of produced networks in these three layers and ECM was investigated, based on various ECM degradation patterns. The generated capillary networks involved the rules of MVB and MVA.

Numerical coupling of avascular growth and angiogenesis process was one of the novelties of this study. Although a similar coupled model has been proposed in the literature [3], our suggested model allowed the extension of some of the results reported in literature [6], since spatial heterogeneity (a three-layered tumor) was introduced in the avascular tumor during angiogenesis.

As the findings indicated, under certain parameter regimes, vascularization penetrates accordingly into the three layers of the tumor. This result was not reported in the study by Anderson et al. [6], since their angiogenesis model did not include different layers of avascular tumor. We also modified the orthogonal sprout branching patterns with forward diagonal branching patterns in the angiogenesis model for more compliance with reality. With this modification, we observed faster progression of sprouts towards the tumor and more realistic structures.

Figure 18 shows both the orthogonal and forward diagonal patterns of sprout branching. As illustrated in this figure, when one of the branched sprouts was placed along the main body (the three last cases in the orthogonal branching pattern), some rebounds could occur, which is rarely observed in *in vivo* experiments.

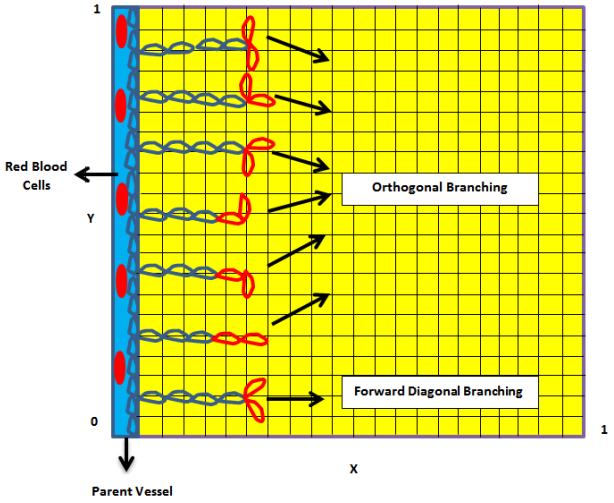

Figure 18. The schematic diagram indicating the comparison between orthogonal and forward diagonal sprout branching

This model provided the basic data which could be useful for future studies. The estimations of MVB and MVA could be used as appropriate indicators for the investigation of treatment effectiveness. It is also interesting

to develop a model to simulate vascular tumor growth and metastasis by modeling the effects of blood flow through the produced capillary networks.

In this model, for simplicity, no delay was assumed between the time when the tumor reached its maximum avascular size and the initiation of angiogenesis. As mentioned earlier, this delay is proportional to TAF diffusion and decay rate and the distance of neighboring blood vessels from the tumor (the factor which can influence even the occurrence of angiogenesis). We also assumed the initial formation of five sprouts, which all started to progress from random positions, simultaneously. These assumptions could be modified in order to model a more realistic process for sprouting angiogenesis. The authors aim to proceed with their research on these two issues. The results will be reported in future studies.

5. Conclusion

In this study, we derived an algorithmic framework for a hybrid model, which coupled a two-dimensional continuous mathematical model for avascular tumor growth with a discrete model of angiogenesis. We performed several numerical simulations by using our algorithms. Our numerical simulations could provide a qualitative comparison between three layers of tumor cells, their TAF-producing abilities and subsequent penetration of micro-vessels. Moreover, we could gain an insight into the dynamics of MVB and MVA in ECM and three different parts of the tumor. This model could provide useful information for understanding the phenomena fundamental to angiogenesis and solid tumor growth in future clinical research. Model predictions were in qualitative agreement with experimental observations and might have implications as a supplementary model to facilitate mathematical analyses for anti-cancer therapies. As mentioned throughout the study, in our proposed coupled model and simulations, all parameter values were selected, based on previous published papers. Also, we cited authentic papers for validation of the results. However, it should be noted that experimental validation using *in vivo* or *in vitro* angiogenesis assays is expensive and time-consuming and requires specialized training. Although *in vitro* assays tend to be more rapid, *in vitro* angiogenesis assays operate on the principle that endothelial cells form tubule-like structures when cultured on a supportive matrix. In fact, assays, involving a matrix, derived from murine tumors and Matrigel, are now the most common *in vitro* tubule formation assays. We aim to conduct further *in vivo* or *in vitro* angiogenesis assays in the future.

References

1. Mantzaris NV, Webb S, Othmer HG. Mathematical modeling of tumor-induced angiogenesis. Journal of mathematical biology. 2004;49(2):111-87.
2. Vilanova G, Colominas I, Gomez H. Capillary networks in tumor angiogenesis: from discrete endothelial cells to phase-field averaged descriptions via isogeometric analysis. Int J Numer Method Biomed Eng. 2013 Oct;29(10):1015-37.
3. Anderson A, Chaplain M, Newman E, Steele R, Thompson A. Mathematical modelling of tumour invasion and metastasis. Computational and Mathematical Methods in Medicine. 2000;2(2):129-54.
4. Hanahan, D, and Weinberg RA. The hallmarks of cancer. Cell. 2000;100(1): 57-70.
5. Hanahan D, Weinberg RA. Hallmarks of cancer: the next generation. Cell. 2011;144(5):646-74.
6. Anderson AR, Chaplain M. Continuous and discrete mathematical models of tumor-induced angiogenesis. Bulletin of mathematical biology. 1998;60(5):857-99.
7. Conway EM, Collen D, Carmeliet P. Molecular mechanisms of blood vessel growth. Cardiovasc Res. 2001 Feb 16;49(3):507-21.
8. Kurz H, Burri PH, Djonov VG. Angiogenesis and vascular remodeling by intussusception: from form to function. News Physiol Sci. 2003 Apr;18:65-70.
9. Figg WD, Folkman J. Angiogenesis: An Integrative Approach from Science to Medicine: Springer, New York; 2011.

10. Qutub A, Gabhann FM, Karagiannis ED, Vempati P, Popel AS. Multiscale models of angiogenesis. Engineering in Medicine and Biology Magazine, IEEE. 2009;28(2):14-31.
11. FolkmanJ,Klagsbrun M,Angiogenicfactors,*Science***235**(4787):442-447, 1987. Folkman J, Klagsbrun M. Angiogenic factors. Science. 1987;235(4787):442-7.
12. Stokes CL, Lauffenburger DA. Analysis of the roles of microvessel endothelial cell random motility and chemotaxis in angiogenesis. J Theor Biol. 1991 Oct 7;152(3):377-403.
13. Magnusson MK, Mosher DF. Fibronectin: structure, assembly, and cardiovascular implications. Arterioscler Thromb Vasc Biol. 1998 Sep;18(9):1363-70.
14. Hynes, R. O. "Fibronectins springer series in molecular biology." 1990.
15. Birdwell CR, Gospodarowicz D, Nicolson GL. Identification, localization, and role of fibronectin in cultured bovine endothelial cells. Proceedings of the National Academy of Sciences. 1978;75(7):3273-7.
16. Jaffe EA, Mosher DF. Synthesis of fibronectin by cultured human endothelial cells. J Exp Med. 1978 Jun 1;147(6):1779-91.
17. Macarak EJ, Kirby E, Kirk T, Kefalides NA. Synthesis of cold-insoluble globulin by cultured calf endothelial cells. Proc Natl Acad Sci U S A. 1978 Jun;75(6):2621-5.
18. Monaghan P, Warburton MJ, Perusinghe N, Rudland PS. Topographical arrangement of basement membrane proteins in lactating rat mammary gland: comparison of the distribution of type IV collagen, laminin, fibronectin, and Thy-1 at the ultrastructural level. Proc Natl Acad Sci U S A. 1983 Jun;80(11):3344-8.
19. Rieder H, Ramadori G, Dienes HP, Meyer zum Buschenfelde KH. Sinusoidal endothelial cells from guinea pig liver synthesize and secrete cellular fibronectin in vitro. Hepatology. 1987 Sep-Oct;7(5):856-64.
20. Sawada H, Furthmayr H, Konomi H, Nagai Y. Immunoelectronmicroscopic localization of extracellular matrix components produced by bovine corneal endothelial cells in vitro. Exp Cell Res. 1987 Jul;171(1):94-109.
21. Schor SL, Schor AM, Bazill GW. The effects of fibronectin on the migration of human foreskin fibroblasts and Syrian hamster melanoma cells into three-dimensional gels of native collagen fibres. J Cell Sci. 1981 Apr;48:301-14.
22. Liotta LA, Rao C, Barsky SH. Tumor invasion and the extracellular matrix. Laboratory investigation; a journal of technical methods and pathology. 1983;49(6):636-49.
23. Stetler-Stevenson WG, Aznavoorian S, Liotta LA. Tumor cell interactions with the extracellular matrix during invasion and metastasis. Annu Rev Cell Biol. 1993;9:541-73.
24. Lawrence J, Steeg P. Mechanisms of tumor invasion and metastasis. World journal of urology. 1996;14(3):124-30.
25. Mignatti P, Rifkin DB. Biology and biochemistry of proteinases in tumor invasion. Physiol Rev. 1993;73(1):161-95.
26. Matrisian LM. The matrix-degrading metalloproteinases. Bioessays. 1992 Jul;14(7):455-63.
27. Thorgeirsson UP, Lindsay CK, Cottam DW, Gomez DE. Tumor invasion, proteolysis, and angiogenesis. Journal of neuro-oncology. 1993;18(2):89-103.
28. Bresch D, Colin T, Grenier E, Ribba B, Saut O. Computational modeling of solid tumor growth: the avascular stage. SIAM Journal on Scientific Computing. 2010;32(4):2321-44.
29. Mahmood MS, Mahmood S, Dobrota D. A numerical algorithm for avascular tumor growth model. Mathematics and Computers in Simulation. 2010;80(6):1269-77.
30. Saleem M, Agrawal T. Complex dynamics in a mathematical model of tumor growth with time delays in the cell proliferation. International Journal of Scientific and Research Publications. 2012;2(6):1-7.
31. Ramis-Conde I, Chaplain MA, Anderson AR. Mathematical modelling of cancer cell invasion of tissue. Mathematical and Computer Modelling. 2008;47(5):533-45.
32. Anderson A, Chaplain MA. A mathematical model for capillary network formation in the absence of endothelial cell proliferation. Applied mathematics letters. 1998;11(3):109-14.
33. Orme ME, Chaplain MA. Two-dimensional models of tumour angiogenesis and anti-angiogenesis strategies. IMA J Math Appl Med Biol. 1997 Sep;14(3):189-205.
34. Levine HA, Sleeman BD, Nilsen-Hamilton M. Mathematical modeling of the onset of capillary formation initiating angiogenesis. J Math Biol. 2001 Mar;42(3):195-238.
35. Sun S, Wheeler MF, Obeyesekere M, Patrick CW, Jr. A deterministic model of growth factor-induced angiogenesis. Bull Math Biol. 2005 Mar;67(2):313-37.
36. Frieboes HB, Jin F, Chuang YL, Wise SM, Lowengrub JS, Cristini V. Three-dimensional multispecies nonlinear tumor growth-II: Tumor invasion and angiogenesis. J Theor Biol. 2010 Jun 21;264(4):1254-78.
37. Bentley K, Mariggi G, Gerhardt H, Bates PA. Tipping the balance: robustness of tip cell selection, migration and fusion in angiogenesis. PLoS Comput Biol. 2009 Oct;5(10):e1000549.
38. Capasso V, Morale D. Stochastic modelling of tumour-induced angiogenesis. J Math Biol. 2009 Jan;58(1-2):219-33.

39. Macklin P, McDougall S, Anderson AR, Chaplain MA, Cristini V, Lowengrub J. Multiscale modelling and nonlinear simulation of vascular tumour growth. J Math Biol. 2009 Apr;58(4-5):765-98.
40. Cai Y, Xu S, Wu J, Long Q. Coupled modelling of tumour angiogenesis, tumour growth and blood perfusion. J Theor Biol. 2011 Jun 21;279(1):90-101.
41. Mitchell AR, Griffiths DF. The finite difference method in partial differential equations: John Wiley; 1980.
42. Lien WM, Ackerman NB. The blood supply of experimental liver metastases. II. A microcirculatory study of the normal and tumor vessels of the liver with the use of perfused silicone rubber. Surgery. 1970 Aug;68(2):334-40.
43. Folkman J. Tumor angiogenesis factor. Cancer Research. 1974;34(8):2109-13.
44. Billy F, Ribba B, Saut O, Morre-Trouilhet H, Colin T, Bresch D, et al. A pharmacologically based multiscale mathematical model of angiogenesis and its use in investigating the efficacy of a new cancer treatment strategy. J Theor Biol. 2009 Oct 21;260(4):545-62.
45. Paku S, Paweletz N. First steps of tumor-related angiogenesis. Lab Invest. 1991 Sep;65(3):334-46.